

Single cell profiling of bronchoalveolar immune cells in checkpoint inhibitor-related pneumonitis

Pengfei Cui

the Fifth Medical Center of PLA General Hospital

Jinfeng Li

the Fifth Medical Center of PLA General Hospital

Haitao Tao

the Fifth Medical Center of PLA General Hospital

Xiaoyan Li

the Fifth Medical Center of PLA General Hospital

Liangliang Wu

Chinese PLA General Hospital & Chinese PLA Medical School

Junxun Ma

the Fifth Medical Center of PLA General Hospital

Huanhuan Wang

the Fifth Medical Center of PLA General Hospital

Di Huang

the Fifth Medical Center of PLA General Hospital

Ziwei Huang

the Fifth Medical Center of PLA General Hospital

Shixue Chen

the Fifth Medical Center of PLA General Hospital

Min Zhang

Academy of Military Medical Sciences

Yi Hu (✉ huyi_0912@126.com)

the Fifth Medical Center of PLA General Hospital

Article

Keywords:

Posted Date: February 24th, 2022

DOI: <https://doi.org/10.21203/rs.3.rs-1341170/v1>

License:  This work is licensed under a Creative Commons Attribution 4.0 International License.

[Read Full License](#)

Abstract

Immune checkpoint inhibitors (ICIs) therapy induced pneumonitis (CIP) complicates this effective in therapy patients with non-small cell lung cancer (NSCLC), but the underlying mechanisms remain incompletely understood. Here, we implemented comprehensive single-cell transcriptome, flow cytometry and cytokine expression analysis to shed light on the complexity of the immunological responses in the bronchoalveolar microenvironment from NSCLC patients with CIP. We demonstrated a dramatic accumulation of CXCL13⁺ CD4 and CD8 T cells with highly cytotoxic and effector functions in CIP. Monocyte differentiation trajectories showed that hyperinflammatory monocytes and LAMP3⁺ dendritic cells (DCs) were enriched in CIP, while anti-inflammatory macrophages were depleted. Multilineages intercellular crosstalk analysis revealed that CIP specific myeloid subsets could recruit and enhance CXCL13⁺ T cells cytotoxic function through CXCL9/10-CXCR3 and IFNGR1/2-IFNG pathway, respectively. Together, our data highlighted the importance of CXCL13⁺ T cells and LAMP3⁺ DCs in CIP pathogenesis, which could be non-invasive biomarkers to monitor CIP.

Introduction

Immune checkpoint inhibitors (ICIs) therapy have been proved to be an effective anti-cancer treatment program in a wide range of human malignancies^{1,2}, however, ICIs therapy can result in inflammatory toxicities, also termed as immune-related adverse events (irAEs) and even fatal adverse events (FAEs)³⁻⁵. The irAEs can affect any human organ system and induce treatment-limiting toxicities, thus posed a series of challenges for ICIs usage⁶⁻⁸. The irAEs usually occur at barrier sites, including the gastrointestinal (GI) mucosa, liver, skin, and lung^{9,10}, and the FAEs were mainly seen in the respiratory system, which is also termed as checkpoint inhibitor associated pneumonitis (CIP)^{11,12}. The incidence of CIP is around 3% to 5% according to clinical trial data^{13,14}, however, the occurrence of CIP may be higher in real-world settings than previously reported^{15,16}. Hence, dynamic assessment of ICIs therapy and effective monitoring of their adverse events are important for reducing the incidence and mortality of irAEs and facilitating cancer immunotherapy.

The clinical and pathognomonic radiologic features of CIP are nonspecific^{17,18}. Additionally, current diagnosis of CIP requires exclusion of other lung injuries, and fundamental knowledge of CIP pathobiology is lacking^{19,20}. Therefore, comprehensively understanding the CIP pathobiology and dissecting the key cellular players and molecular pathways underlying CIP initiation is critical for cancer immunotherapy, precision diagnosis and timely prevent of CIP.

Single-cell RNA-sequencing (scRNA-seq) is a powerful technology, which is widely used to reveal the heterogeneous cellular and molecular characteristics of various cells associated with cancer and inflammatory disease such as COVID-19 and cancer immunotherapy induced colitis²¹⁻²³. A recent study of comprehensive single-cell immune atlas revealed colitis associated cell populations and the mechanisms of inflammatory toxicities induced by ICIs therapy²¹. Based on systematic single-cell

profiling of Bronchoalveolar lavage fluid (BALF), researchers uncovered the molecular characteristics associated with COVID-19 immunopathology^{22,24}. What remains unknown is the key cellular players and molecular pathways associated with CIP initiation.

Here, we implemented scRNA-seq to shed light on the complexity of the immunological responses in the BALF immune microenvironment from non-small cell lung cancer (NSCLC) patients with CIP. We used complementary methods and cohorts, including flow cytometry and luminex to identify the cells and cytokine that regulate CIP. Some of the results of this study have been previously reported in the form of abstracts. Together, this approach led to discovery of cellular and molecular marker to predict the development of the CIP as well as the identification of the BALF as a potential regular procedure to monitor this lung AEs activity.

Results

Global analysis of immune cell populations in CIP

We present the first in-depth cellular and molecular analysis of immune cell populations in CIP induced by ICIs therapy, which enrolled in three patient populations from 12 donors: (1) ICI-treated NSCLC patients with CIP (n = 6, CIP(+)); (2) ICI-treated NSCLC patients without CIP (n = 3, CIP(-)); and (3) healthy adults (n = 3, Healthy control, GSE145926) (Fig. 1a-b). Our study design allowed us to distinguish key cellular players, molecular pathways, and effector programs induced by drug exposure to dissect CIP pathophysiology. All ICI-treated patients had been previously treated with PD-1/PD-L1 blockade (Fig. 1b, Supplementary Table 1 and 2). BALF was obtained immediately after development of CIP (average of 3.67 days, maximum of 8 days) from the new infiltrated area (Supplementary Table 1). All patients in donor cohort received corticosteroids after bronchoscopy (Supplementary Table 3). A total of 78,027 high-quality cells passed data quality control (Supplementary Fig. 1a), and 28 cell clusters were obtained after integrated bioinformatics analysis including data integration, normalization, batch effect removal, dimension reduction, and clusters detection (Methods). We identified and annotated 17 cell sub-types according to the expression of canonical gene markers, which were composed of ciliated cell (SCGB3A1, CAPS), secretory cell (LCN2), CD8⁺T cell (CD3D, CD8A), CD4⁺ T cell (CD4), regulatory T (Treg) cell (CD4, FOXP3), natural killer (NK) cell (XCL2), plasma B cell (MZB1, JCHAIN), B cells (CD79A, CD79B), proliferating cell (MKI67, TOP2A), dendritic cell (DC) (CD1C, CLEC9A, LAMP3), monocyte/macrophage (S100A9, APOE, MARCO) (Fig. 1c-d, Supplementary Fig. 1b). Each cell subtypes contained cells from all patients, indicating the absence of major patient-specific batch effects (Fig. 1e, Supplementary Fig. 1c). The percentage of each cell subtypes differed largely in three patient groups (Fig. 1f-g, Supplementary Fig. 1d), indicated that drug exposure could lead to immune microenvironment alteration dramatically. The scRNA-seq findings revealed an increase in the frequency of T/NK (cluster 4-7) and proliferative or cycling cells (cluster 10) in CIP(+) group while the monocyte/macrophages (cluster 14-17) were depleted (Fig. 1h), which was validated by flow cytometry analysis in another patient cohort (Fig. 1i, CIP(+), n=5;

CIP(-), n=4, Supplementary Table 4 and 5). These results demonstrated that CIP is highly associated with major changes in the immune microenvironment in the BALF.

Characteristics and dynamics of CD8⁺ T cell in CIP(+) BALF

We next performed further detailed clustering of CD8⁺ T cells and generated eight CD8⁺ T subtypes (Fig. 2a), annotated as CD8-ZNF683 (CD8-Trm), CD8-APOC1, CD8-GZMK, CD8-PRF1, CD8-CXCL13, CD8-IFIT, and cycling cell subtypes: CD8-MCM7, CD8-MKI67 (Fig. 2b). The overall organization of the CD8⁺ T cell compartment showed striking differences between control group and CIP(+) group (Fig. 2c). CIP(+) group was enriched in five CD8⁺ T cell subtypes, including CD8-ZNF683, CD8-GZMK, CD8-PRF1, CD8-CXCL13, and CD8-MCM7 (Fig. 2d), which was validated by flow cytometry analysis at the protein level (Fig. 2e). The CD8-CXCL13 not only exhibited a higher expression level of exhaustion makers CXCL13, LAG3, and PDCD1, but also expressed high level of IFNG, GNLY, and GZM family members, which could be defined as activated T cells, and has been recently reported to predict effective responses to PD-L1 blockade^{25,26}. Of note, CIP(+) enriched CD8⁺ T cell clusters expressed high level of immune checkpoint molecules TIGIT, CTLA4, PDCD1, HAVCR2 (TIM3) and LAG3 (Fig. 2f), indicated that CIP(+) patients may benefit from ICIs therapy. Also, the CIP(+) enriched CD8⁺ T cells had a higher expression level of cytotoxic markers such as GZMA, GZMB, GZMK, GZMM, GZMH, PRF1, NKG7, and GNLY (Fig. 2g, $p < 2.2e-16$), which is also the main significant changes of CD8⁺ T cells in CIP(+) versus CIP(-) samples (Fig. 2h), these results indicated a highly cytotoxic and effective environment induced by ICIs. To investigate the origin of CD8-CXCL13, we performed trajectory analysis and TCR clone analysis. The pseudo time trajectory analysis showed a potential differentiation trajectory from CD8-ZNF683 (CD8-Trm) to CD8-CXCL13 (Fig. 2i-j), which is consistent with the result that colitis associated CD8-Trm contribute to cytotoxic CD8 T cells²¹. TCR clone expansion analysis also showed that CD8-CXCL13 shared similar clone expansion compared with CD8-ZNF683, which demonstrated a dynamic transcriptomic phenotype transition between CD8-CXCL13 and CD8-ZNF683 in CIP. Together, these results indicated an important role of CD8-ZNF683 and dramatic elevation of CD8-CXCL13 in CIP.

Characteristics and dynamics of CD4⁺ T cell in CIP(+) BALF

Sub-clustering of total CD4⁺ T cells generated seven CD4⁺ T subtypes (Fig. 3a), annotated as CD4-STMN1, CD4-CXCL13, CD4-GZMK, CD4-CD40LG, CD4-IFIT, CD4-IL7R, and Treg according to the top 10 differentially expressed genes (DEGs) and transcriptomic factors (TFs) (Fig. 3b-c). Only one healthy sample (H2) didn't detect CD4⁺ T cells (Fig. 3d) and the CD4-IL7R, naïve CD4⁺ T cells were predominated in health control and the frequencies was decreased in CIP(+) group dramatically (Fig. 3e). CD4-GZMK, CD4-IFIT and CD4-CXCL13 were enriched in CIP(+) group (Fig. 3e), and the percentage of these cell subtypes in CIP BALF was validated by flow cytometry analysis at the protein level (Fig. 3f). Consistent with CD8-CXCL3, CD4-CXCL13 exhibited high expression of exhaustion markers PDCD1, CXCL13, LAG3, and T cell cytotoxic and effector markers IFNG, GNLY, and GZMA (Fig. 3b). Additionally, the CIP(+) enriched CD4⁺ T cells expressed a high level of cytotoxic markers such as GZMA, GZMB, GZMK, GZMM, GZMH, PRF1, NKG7, and GNLY, indicated their anti-tumor activity (Fig. 3g, $p < 2.2e-16$). Further cellular

differentiation trajectory analysis revealed that naïve CD4 T cells (CD4-IL7R) not only contributed to CD4-CXCL13, CD4-GZMK, but also Treg cell, indicated that transition of naïve CD4 T cells (CD4-IL7R) may be the most obvious signal reflecting changes in the CIP microenvironment (Supplementary Fig. 2a-c). We also investigated the Treg phenotype diversity and obtained four Treg subtypes following sub clustering of all Treg cells, with the Treg-IFIT and Treg-LAG3 expanded in CIP(+) group (Fig. 3h). Meanwhile, the CIP(+) associated Treg subtypes enriched IFN- α , IFN- γ , TNF, and inflammatory pathways and exhibited a high level of IFN characteristic genes such as IFIT1, IRF1, IFI6, and IRF6 (Fig. 3i,3j). Since IFN- γ related mRNA profile is related to clinical response to PD-1 blockade²⁷, these results indicated CIP(+) associated Treg subtypes were associated with better response to ICIs therapy.

Gene expression programs of CIP-associated T cell subpopulations

As the expression of immune inhibitory receptors determines the efficacy of ICIs therapy, we further investigated the expression of inhibitory receptors and explored the alternated gene expression programs in CIP-associated CD8 (Fig. 4a-d) and CD4 (Fig. 4e-h) T cell subpopulations. Sub-cluster analysis of CD8 and CD4 T cells revealed that T cell exhaustion genes CXCL13, PDCD1 (PD-1), CTLA4, TIGIT, HAVCR2 (TIM-3) and LAG3 were specifically expressed in CIP-associated T cell subpopulations (CD8-CXCL13, and CD4-CXCL13) (Fig. 4b,4c; Fig. 4f,4g). At the protein level, an increased percentage of CD8 and CD4 T cells expressed CXCL13 and PD1 in CIP(+) group compared with control subjects (Fig. 2e, Fig. 3f). We also evaluated the most DEGs in CIP-associated clusters, and found the cytotoxicity genes GZMB and XCL1 (CD8⁺ T cells) and GZMA, GZMK, IFNG, GNLY (CD4⁺ T cells) were the top DEGs in CIP-associated clusters (Fig. 4d, 4h). We also found that chemokines receptor CXCR6 was the top DEGs in CIP-associated CD4 clusters (Fig. 4h). These results demonstrated that dramatic expansion and activation of CXCL13⁺ T cells lead to CIP pathogenesis.

Hyper-inflammatory phenotype of myeloid cells expanded in CIP(+) BALF

Myeloid cells phenotype related molecular characteristic and differentiation trajectories abnormalities has been reported to be associated with COVID-19 and other disease²⁸. In this study, myeloid cells accounted over 50% of total sequencing cells, which could be classified into ten cell subtypes and annotated as Mono1, Mono2, Mono/Mac1, Mono/Mac2, Mac1, Mac2, DC-CLEC9A, DC-CD1C, DC-LAMP3, and Mac-Cycling according to the top 10 DEGs and TFs (Fig. 5a-c) and the proportion of these cell subtypes differed in patients (Fig. 5b). The CIP(+) samples were enriched in three myeloid cell subtypes DC-LAMP3, Mono1, Mono2 (Fig. 5d, Supplementary Fig. 3a), and all of which exhibited high expression level of interferon genes IFITM1, IFITM3 and chemokines CCL2, CCL4, CXCL9, and CXCL10 (Fig. 5c). These cells also enriched inflammatory signaling pathway such as IFN- α , IFN- γ , TNF (Fig. 5e, Supplementary Fig. 3b-c). Previous studies reported that the DC-LAMP3 was mature DC, can migrate from tumor to lymph nodes²⁹. In this study, DC-LAMP3 not only exhibited high M1 signature score, but also had strong migration and activation score (Fig. 5f, Supplementary Table 6), indicated that DC-

LAMP3 may migrate from tumor tissue to BALF, and provided a hyper-inflammatory environment, which could be potential biomarkers to screen CIP. Additionally, CIP(+) specific myeloid cells showed high expression of CXCL9, CXCL10 (Fig. 5g) compared with myeloid cells from CIP(-) clusters, which is also validated by chemokines assay (Supplementary Fig. 3d-e, Supplementary Table 7). As high expression level of CXCL9, CXCL10 encoded chemokines that recruit CXCR3⁺ or CXCR6⁺ effector T cells to sites of inflammation³⁰, we therefore supposed that DC-LAMP3 may be key cellular player to recruit effector T cells, thus lead to CIP pathogenesis. Further cellular differentiation trajectory analysis revealed that the DC-LAMP3 was derived from monocytes (Fig. 3h, Supplementary Fig. 3f), these results demonstrated hyper-inflammatory phenotype of myeloid cells inhabited in CIP(+) pulmonary alveoli, highlighted the potential role of DC-LAMP3 and monocytes in promoting effector T cells accumulation and cytotoxicity in the CIP microenvironment.

Multi-lineage intercellular crosstalk and potential therapeutic targets for CIP

Having defined CIP associated T cells and myeloid cells subpopulation, we performed an unbiased ligand-receptor interaction analysis between these populations to explore multi-lineage intercellular crosstalk within the CIP BALF. Numerous statistically significant ligand-receptor pairs and signaling pathway networks were detected (Fig. 6a-c, Supplementary Fig. 4a-h). Interestingly, CIP(+) groups exhibited more significant ligand-receptor pairs than CIP(-) group, and DC-LAMP3 showed close interaction links with CXCL13⁺ T cells. Specifically, immune inhibitor PD-L1, PD-L2, and TIGIT signaling pathway and CD80 signaling pathway networks were enriched in CIP(+) group (Fig. 6b) between CXCL13⁺ T cells, cytotoxic T cells and DC-LAMP3 subpopulation (Fig. 6b-f). Previous studies reported that the level of PD-L1 expression by macrophages and DCs may be more closely related to the ICIs efficacy³¹. In this study, CIP(+) group exhibited elevated of immune inhibitor PD-L1, PD-L2, and TIGIT signaling than CIP(-) groups, indicated that CIP(+) group may benefit more from ICIs therapy (Fig. 6b, Supplementary Fig. 5a,5b). Also, the CIP associated T cells expressed high level of chemokine receptor genes CXCR4, and CXCR6 (Fig. 6h), with the myeloid cell ligand CXCL9, and CXCL10 expressed in hyper-inflammatory DC-LAMP3 (Fig. 6g). Therefore, the DC-LAMP3 contributed effector and cytotoxic T cell recruitment through CXCL, and CCR signaling pathway networks (Fig. 6f). Interestingly, we also observed that CIP associated T cells expressed high level of IFNG (Fig. 6e, Fig. 6g), with the receptors IFNGR1, and IFNGR2 also highly expressed in DC-LAMP3, and monocytes (Fig. 6e, Fig. 6h), we might speculate that blockade of inhibitor signaling pathway in DC-LAMP3 enhanced the efficacy and cytotoxic of T cells through IFN pathway, thus lead to CIP (Fig. 6e-h). Together, our unbiased dissection of the key ligand-receptor interactions between CIP-associated hyper-inflammatory myeloid cells and T cells highlights PD-L1, PD-L2, TIGIT, IFN, CCL, and CXCL signal axis as important regulators within the BALF microenvironment of CIP patients.

Discussion

The irAEs caused by ICIs can complicate this effective therapy and limit its use in patients with cancer^{32,33}. Underling the precise pathophysiology associated with irAEs is critical to develop non-invasive diagnostic and therapeutic strategy for CIP. Currently, the diagnosis of CIP remains to be an exclusionary diagnosis³⁴⁻³⁷. Bronchoscopy can be helpful to establish diagnosis, particularly if alternative aetiologies are under consideration^{32,37}. However, bronchoscopy biopsy as a main method to diagnosis the interstitial lung disease remains to be invasive and cannot be performed more than once^{37,38}. In this study, we employed the BALF, a non-invasive reproducible sampling method, and generated a comprehensive and systematic single-cell transcriptomic atlas of CIP. We identified key cellular players, molecular pathways, and effector programs associated with CIP. Additionally, the pseudotime trajectories for both T-cells and myeloid cells, and TCRαβ analysis demonstrated the cellular differentiation programs and clone similarity associated with CIP.

Specifically, our analyses revealed that activated and cytotoxic cellular subpopulation such as CXCL13⁺ T cells, IFIT⁺ T cells, IFIT⁺ Treg, effector T cells, monocytes, and LAMP3⁺ DC expanded in CIP(+) group, while the naïve T cells and anti-inflammatory M2 macrophage were depleted. CIP(+) enriched cellular subpopulation displayed potent interferon alpha response and acute immune response signature such as upregulation of IL2, IL6, and TNF signaling pathway, indicated that the innate immune system has been activated by ICIs therapy. Additionally, cellular trajectories and TCRαβ clone analysis demonstrated that the activated CD8-CXCL13 and effector CD8 T cells originated from CD8-Trm with tissue resident signature, also the naïve CD4 T cells differentiate to Treg, CD4-CXCL13, and effector CD4 T cells, which highlighted the important role of cellular phenotypical transition alongside with CIP initiation and progression. Recent studies showed that the elevated frequencies and activation of CXCL13⁺ T cells were associated with the effective responses to the ICIs therapy^{26,39,40}. Herein, CXCL13⁺ T cells exhibited high level of immune checkpoint molecules such as PDCD1, TIGIT, CD38, CTLA4, and HAVCR2, indicated that CIP(+) patients would have more effective response with ICIs therapy than patients without CIP, which is consistent with a clinical phenomenon observed by our team that CIP patients may have a better ICIs efficacy than patients without CIP⁴¹. Meanwhile, CD4 and CD8 T cells exhibited a high expression level of cytotoxic marker and effector factors such as Granzyme (GZM) family, PRF1, NKG7, and GNLY in CIP(+) samples compared with CIP(-) samples. Our study revealed that CXCL13⁺ T cells were associated with ICIs therapy responses and ICIs induced CIP, which may be potential diagnostic biomarkers for CIP. Importantly, Treg subtype analysis revealed that these CIP associated Treg cells exhibited activation of INF-α, INF-γ, TNF-α, and IL-2 signal pathway, which is similar with fragile Tregs that may maximize efficacy and improve patient response to immunotherapy⁴². This indicated that these Treg cells were also activated by ICIs and the negative immune regulation was inhibited, which highlighted the important role of Treg in CIP.

Current research suggests that inhibition of the PD1-PDL1 pathway not only blocks immunosuppression within the tumor, but that several important peripheral cells are also involved and correlate with the degree of response to treatment^{31,43,44}. The conventional wisdom is that the efficacy of ICIs is related to the level of PDL1 expression by tumor cells, however, the level of PDL1 expression by antigen-presenting

cells (including macrophages and DCs) may be more closely related to the degree of patient response to ICIs^{31,44}. In this study, CIP associated LAMP3⁺ DCs not only expressed high level of exhaustion markers CD274 (PDL1), and PDCD1LG2 (PDL2), but also high level of CXCL9, CXCL10, CXCL16, CCL2, CCL17, IFNGR1, and IFNGR2. The expression of CXCL9, CXCL10, and CCL2 were also validated by flow cytometry and cytokines assay. CCL2 is a superfamily of secreted proteins involved in immunoregulatory and inflammatory processes⁴⁵, CXCL9 and CXCL10, the ligands for CXCR3 and induced by IFN γ , have been shown to be important for recruiting effector T cells to tumors, which would be expected to have positive effects on anti-tumor immunity³⁰. Intercellular crosstalk analysis revealed that LAMP3⁺ DCs interacted closely with CXCL13⁺ T cells subpopulation through PD-1, PD-L1, TIGIT, CTLA-4, CXCR, and IFN pathway. We therefore speculate that blockade of PDL1 or PDL2 lead to LAMP3⁺ DCs activation and recruit effector T cells to site of inflammation through CXCL9/10-CXCR3 pathway, and thus enhance ICIs effective response, but also lead to CIP through IFNGR1/2-IFNG pathway. Importantly, the monocyte to LAMP3⁺ DCs trajectories revealed that percentage of LAMP3⁺ DCs with hyperinflammatory and migratory features significantly elevated in CIP. Interestingly, LAMP3⁺ cDCs, the mature DC type, has been reported to be of high capacity of migratory ability^{29,46}, which can migrate from tumors to hepatic lymph nodes²⁹. Together with our results, we speculate that LAMP3⁺ DCs may migrate from the lung tumor site to the BALF, which could be potential liquid biomarker for monitoring CIP. The clinical relevance of these findings needs to be addressed, correlating the phenotype of this type of DCs with the occurrence of CIP or effective response of the patients treated with ICIs. Because performing BALF to obtain BALF as a non-invasive procedure is simple and safe, the potential use of BALF-derived myeloid cells as CIP diagnostic biomarkers should be further explored.

Our study has several shortcomings, including limited and heterogeneous patients and a lack of longitudinal samples collected before and after the CIP occur, thus preclude adjustment for clinical comorbidities (such as chronic obstructive pulmonary disease) that may confound our results. In addition, while only patients with a negative infectious work-up were included in the CIP cohort, it is possible that BALF cultures did not identify a focus of infection in patients thought to have CIP. Lastly, although BALF of CIP infiltrates were performed in areas not previously affected by tumor, it is possible that presence of malignancy in the nearby airways may could have influenced our results. Nevertheless, this landscape of bronchoalveolar immune cells reveals an in-depth understanding of mechanisms underlying immunopathogenesis in CIP and further supports the possibility of using immune cells in the BALF as biomarkers in the prediction of CIP and anti-tumor immunity.

In conclusion, this landscape of bronchoalveolar immune cells reveals aberrant T cell and myeloid cell responses underlying immunopathogenesis in CIP. Our analysis uncovers the potential mechanism that support the clinical observation that CIP is correlated with better ICIs efficacy⁴¹. Our data also provide a hypothesis-generating insight into the possibility of using BALF as a non-invasive procedure to predict the occurrence of CIP as well as the efficacy of ICIs. Taken together, our study can be a valuable resource for further investigation to gain deeper biological insights that will lead to novel biomarkers of CIP and the response for current immunotherapies for NSCLC.

Methods

This study was conducted according to the principles expressed in the declaration of Helsinki. Ethical approval was obtained from the Ethics Committee of the Chinese People's Liberation Army General Hospital with number S2018-092-01. All participants provided written informed consent for sample collection and subsequent analyses.

Study population.

Patients were enrolled in this prospective observational study if they were diagnosed with NSCLC and treated with ICIs. BALF was collected whenever patients underwent bronchoscopy. The sample was obtained before initiating steroids and antibiotics. A clinical diagnosis of CIP was adjudicated by the multidisciplinary irTox team (information to follow). If CIP was diagnosed, the BALF sampled was categorized as "CIP". After adjudication, patients with CIP were treated with high-dose steroids (1 mg/kg prednisone). Second-line agents (Tocilizumab) were added at the discretion of the treating team if no improvement was noted after 72 hours.

CIP diagnosis.

CIP was defined as shortness of breath, decreased exercise tolerance, exertional desaturation, and/or cough along with the presence of new radiographic infiltrates and lack of evidence of infection (negative cultures on BALF, negative respiratory viral swab) or alternate etiologies (diffuse alveolar hemorrhage, heart failure)³⁴. Radiographic assessment was performed based on response evaluation criteria in solid tumors (RECIST); cases where the new infiltrates were deemed to represent tumor progression were excluded from both control and CIP groups. A diagnosis of CIP was adjudicated following review and discussion of the pertinent microbiologic and radiographic^{15,47} data by 2 oncologists, and a radiologist. Patients in whom clinical equipoise regarding infection was present (e.g., clinical presence of fever, purulent sputum, sick contacts, elevated bands on complete blood count differential) were not adjudicated as CIP even if the BALF cultures were negative.

BALF collection.

In control patients, the middle lobe was lavaged. In patients with CIP, an area with new infiltrates not to be associated with tumor was lavaged. The volume of instilled and returned saline was abstracted from the BALF procedure note. BALF specimens were processed with ammonium chloride–potassium lysis solution.

Isolation of BALF cells.

Approximately 20 ml of BALF was obtained and placed on ice. BALF was processed within 2 h. After passage of BALF through a 100- μ m nylon cell strainer to remove clumps and debris, the supernatant was centrifuged and the cells were re-suspended in cooled RPMI 1640 complete medium. The supernatant samples were collected and stored at -80°C until use.

Single cell sequencing and pre-processing data

We prepared the single-cell RNA-seq and TCR libraries on the Chromium platform (10× Genomics), using the Chromium Next GEM Single Cell 5' Kit v2. The FACS sorting live cells (7-AAD negative) were pooled together and washed with RPMI-1640 three times and concentrated to 600–1000 cells per μL and then immediately before loading on the 10× microfluidic chip (10x Genomics) following the manufacturer's protocol to generate a complementary deoxyribonucleic acid (cDNA) library. Amplified cDNA was then used for both 50 gene expression library construction and TCR V(D)J targeted enrichment performed with the Chromium Single Cell V(D)J Enrichment Kit, Human T cell (10x Genomics), followed by V(D)J library construction. The raw sequencing data were aligned to the GRH38 reference genome using cellranger (10X Genomics, v4) count and vdj function. The count matrices of gene expression from each sample were imported to Seurat⁴⁸. We selected high quality cells for further analysis following three measurements: 1) cells had either over than 2001 unique molecular identifiers (UMIs), fewer than 6,000 or over than 301 expressed genes, or fewer than 10% UMIs derived from the mitochondrial genome; 2) genes expressed in over than ten cells in a sample; 3) cell doublets were removed using DoubletFinder⁴⁹ R package. The cells-by-genes expression matrices of the remaining high-quality cells were integrated with the RunFastMNN function provided by SeuratWrappers R package and then normalized to the total cellular UMI count. A union of the top 2,000 genes with the highest dispersion for each data set to generate an integrated matrix. We then performed data normalization, dimension reduction, clusters detection as previously reported. Briefly, the gene expression matrices were scaled by regressing out the total cellular UMI counts and percentage of mitochondrial gene. The principal component analysis (PCA) was conducted using highly variable genes (HVGs), and the top 30 significant principal components (PCs) were selected to perform Uniform Manifold Approximation and Projection (UMAP) dimension reduction and visualization of gene expression. We annotated cell sub-cluster with similar gene expression pattern as same cell type and cell types in the resulting two-dimensional representation were annotated to known biological cell types using canonical marker genes.

Trajectory analysis

To explore the potential differentiation routines between CD4, and myeloid cells subtypes, we performed the trajectory analysis via the monocle⁵⁰ R package as previously reported. Firstly, we constructed the monocle object using "newCellDataSet" function and the DEGs calculated via "differentialGeneTest" function were selected for trajectory analysis. Then "DDRTree" function was used for dimensionality reduction and "plot_cell_trajectory" function for visualization. For CD8 subtype trajectory inference analysis, the R package Slingshot⁵¹ was used and PCA-based dimension reduction was performed with differentially expressed genes, followed by two-dimensional visualization with UMAP.

GSEA analysis

To illustrate the enriched signaling pathways of all sequencing cells and myeloid subtypes, we employed the GSEA⁵² package to assess the pathway differences using the Hallmark gene set provide by the

Molecular Signatures Database (MSigDB), which were calculated with a linear model offered by the limma package.

Intercellular crosstalk

We employed Cellchat⁵³ package (v0.0.2) to infer the intercellular communication, following a standard pipeline implemented in R could be found in <https://github.com/sqjin/CellChat>. We firstly set ligand-receptor interaction list in human and projected the gene expression data onto the protein-protein interaction (PPI) network by identifying the over-expressed ligand-receptor interactions. To obtain the biologically significant cell-cell communications, probability values for each interaction were calculated by performing permutation tests. The inferred intercellular communication network of each ligand-receptor pair and each signaling pathway was summarized and visualized by circle plots and heatmap.

Cytokine measurement by Luminex and statistic.

The cytokines including 6Ckine / CCL21, BCA-1 / CXCL13, CTACK / CCL27, ENA-78 / CXCL5, Eotaxin / CCL11, Eotaxin-2 / CCL24, Eotaxin-3 / CCL26, Fractalkine / CX3CL1, GCP-2 / CXCL6, GM-CSF, Gro- α / CXCL1, Gro- β / CXCL2, I-309 / CCL1, IFN- γ , IL-1 β , IL-2, IL-4, IL-6, IL-8 / CXCL8, IL-10, IL-16, IP-10 / CXCL10, I-TAC / CXCL11, MCP-1 / CCL2, MCP-2 / CCL8, MCP-3 / CCL7, MCP-4 / CCL13, MDC / CCL22, MIF, MIG / CXCL9, MIP-1 α / CCL3, MIP-1 δ / CCL15, MIP-3 α / CCL20, MIP-3 β / CCL19, MPIF-1 / CCL23, SCYB16 / CXCL16, SDF-1 α + β / CXCL12, TARC / CCL17, TECK / CCL25, TNF- α were detected in CIP(+) and CIP(-) BALF samples according to the instruction (Bio-Rad, Bio-Plex Pro™ Human Chemokine Panel, 40-Plex), each group contains more than 5 samples. The expression matrix of cytokines was scaled and clustered using complete linkage clustering and Euclidean distance by heatmap. The student t tests were used to compare mean differences between control and CIP cytokine values. A p value less than 0.05 was accepted as significant.

Flow cytometry

In order to validate the scRNA-seq findings, the following antibodies were used to label the CXCL13+ CD4 and CD8 T cells: CD45 (BV421, 563879 BD, lot 9066960), CD3-BV421, CD4-PE-CY7, CD8-APC-750, CD19-Per-cp, CD103-APC, PD-1-PE. The Treg cells were labeled using CD45-BV510, CD3-BV421, CD4-PE-CY7, CD8-APC-750, CD25-PE, Foxp3-PE-CY5, IFN- γ -APC. The LAMP3+ DC were labeled using CD45-BV510, CD11c-FITC, CD68-PE, CD163-BV421, PD-L1-APC-CY7, LAMP3-APC. Stained cells were detected using BD FACSCanto™ and analyzed using FlowJo software.

Data availability

The raw and processed scRNA-seq data of the six CIP(+) and three CIP(-) samples can be accessed in the Gene Expression Omnibus (GEO) database under accession code GSE***. The scRNA-seq data of three healthy BALF controls were acquired from the GEO database under accession code GSE145926, which contains data of three fresh BALF (GSM4475048, GSM4475049, GSM4475050).

Declarations

Acknowledgments

The authors disclosed receipt of the following financial support for the research, authorship, and/or publication of this article: This work was supported by the National Key R&D Program of China (grant number 2017YFC0907904 to Y.H.). The authors declare that there is no conflict of interest.

Author Contributions

P.F.C., M.Z. and Y.H. conceived and designed the study. P.F.C., J.F.L., H.T.T, and X.Y.L. collected the data. M.Z., P.F.C. J.F.L. and L.L.W. analyzed the data. M.Z. and P.F.C. drafted the manuscript. M.Z. and Y.H. revised the manuscript. All authors have reviewed and approved the manuscript.

Competing interests

The authors declare no competing interests.

References

- 1 Thompson, J. A. New NCCN Guidelines: Recognition and Management of Immunotherapy-Related Toxicity. *J Natl Compr Canc Netw* **16**, 594-596, doi:10.6004/jnccn.2018.0047 (2018).
- 2 Carlino, M. S., Larkin, J. & Long, G. V. Immune checkpoint inhibitors in melanoma. *Lancet* **398**, 1002-1014, doi:10.1016/s0140-6736(21)01206-x (2021).
- 3 Tan, P. S., Aguiar, P., Jr., Haaland, B. & Lopes, G. Comparative effectiveness of immune-checkpoint inhibitors for previously treated advanced non-small cell lung cancer - A systematic review and network meta-analysis of 3024 participants. *Lung Cancer* **115**, 84-88, doi:10.1016/j.lungcan.2017.11.017 (2018).
- 4 Jiang, T., Zhou, C., Hu, J. & Song, Y. Combination immune checkpoint inhibitors with platinum-based chemotherapy in advanced non-small cell lung cancer: what's known and what's next. *Transl Lung Cancer Res* **8**, S447-s450, doi:10.21037/tlcr.2019.11.10 (2019).
- 5 Michot, J. M. *et al.* Immune-related adverse events with immune checkpoint blockade: a comprehensive review. *Eur J Cancer* **54**, 139-148, doi:10.1016/j.ejca.2015.11.016 (2016).
- 6 Larkin, J. *et al.* Combined Nivolumab and Ipilimumab or Monotherapy in Untreated Melanoma. *N Engl J Med* **373**, 23-34, doi:10.1056/NEJMoa1504030 (2015).
- 7 Postow, M. A. *et al.* Nivolumab and ipilimumab versus ipilimumab in untreated melanoma. *N Engl J Med* **372**, 2006-2017, doi:10.1056/NEJMoa1414428 (2015).

- 8 Postow, M. A., Sidlow, R. & Hellmann, M. D. Immune-Related Adverse Events Associated with Immune Checkpoint Blockade. *N Engl J Med* **378**, 158-168, doi:10.1056/NEJMra1703481 (2018).
- 9 Dougan, M. & Pietropaolo, M. Time to dissect the autoimmune etiology of cancer antibody immunotherapy. *J Clin Invest* **130**, 51-61, doi:10.1172/jci131194 (2020).
- 10 Darnell, E. P., Mooradian, M. J., Baruch, E. N., Yilmaz, M. & Reynolds, K. L. Immune-Related Adverse Events (irAEs): Diagnosis, Management, and Clinical Pearls. *Curr Oncol Rep* **22**, 39, doi:10.1007/s11912-020-0897-9 (2020).
- 11 Zhao, B., Zhao, H. & Zhao, J. Fatal adverse events associated with programmed cell death protein 1 or programmed cell death-ligand 1 monotherapy in cancer. *Ther Adv Med Oncol* **12**, 1758835919895753, doi:10.1177/1758835919895753 (2020).
- 12 Gomatou, G., Tzilas, V., Kotteas, E., Syrigos, K. & Bouros, D. Immune Checkpoint Inhibitor-Related Pneumonitis. *Respiration* **99**, 932-942, doi:10.1159/000509941 (2020).
- 13 Khunger, M. *et al.* Incidence of Pneumonitis With Use of Programmed Death 1 and Programmed Death-Ligand 1 Inhibitors in Non-Small Cell Lung Cancer: A Systematic Review and Meta-Analysis of Trials. *Chest* **152**, 271-281, doi:10.1016/j.chest.2017.04.177 (2017).
- 14 Forde, P. M., Chaft, J. E. & Pardoll, D. M. Neoadjuvant PD-1 Blockade in Resectable Lung Cancer. *N Engl J Med* **379**, e14, doi:10.1056/NEJMc1808251 (2018).
- 15 Suresh, K. *et al.* Pneumonitis in Non-Small Cell Lung Cancer Patients Receiving Immune Checkpoint Immunotherapy: Incidence and Risk Factors. *J Thorac Oncol* **13**, 1930-1939, doi:10.1016/j.jtho.2018.08.2035 (2018).
- 16 Shibata, Y., Murakami, S. & Kato, T. Overview of checkpoint inhibitor pneumonitis: incidence and associated risk factors. *Expert Opin Drug Saf* **20**, 537-547, doi:10.1080/14740338.2021.1898584 (2021).
- 17 Wang, H. *et al.* Clinical diagnosis and treatment of immune checkpoint inhibitor-associated pneumonitis. *Thorac Cancer* **11**, 191-197, doi:10.1111/1759-7714.13240 (2020).
- 18 Larsen, B. T. *et al.* Clinical and Histopathologic Features of Immune Checkpoint Inhibitor-related Pneumonitis. *Am J Surg Pathol* **43**, 1331-1340, doi:10.1097/pas.0000000000001298 (2019).
- 19 Puzanov, I. *et al.* Managing toxicities associated with immune checkpoint inhibitors: consensus recommendations from the Society for Immunotherapy of Cancer (SITC) Toxicity Management Working Group. *J Immunother Cancer* **5**, 95, doi:10.1186/s40425-017-0300-z (2017).
- 20 Zhai, X. *et al.* The mechanism and risk factors for immune checkpoint inhibitor pneumonitis in non-small cell lung cancer patients. *Cancer Biol Med* **17**, 599-611, doi:10.20892/j.issn.2095-3941.2020.0102 (2020).

- 21 Luoma, A. M. *et al.* Molecular Pathways of Colon Inflammation Induced by Cancer Immunotherapy. *Cell* **182**, 655-671 e622, doi:10.1016/j.cell.2020.06.001 (2020).
- 22 Liao, M. *et al.* Single-cell landscape of bronchoalveolar immune cells in patients with COVID-19. *Nat Med* **26**, 842-844, doi:10.1038/s41591-020-0901-9 (2020).
- 23 Zhang, J. Y. *et al.* Single-cell landscape of immunological responses in patients with COVID-19. *Nat Immunol* **21**, 1107-1118, doi:10.1038/s41590-020-0762-x (2020).
- 24 Wauters, E. *et al.* Discriminating mild from critical COVID-19 by innate and adaptive immune single-cell profiling of bronchoalveolar lavages. *Cell Res* **31**, 272-290, doi:10.1038/s41422-020-00455-9 (2021).
- 25 Leader, A. M. *et al.* Single-cell analysis of human non-small cell lung cancer lesions refines tumor classification and patient stratification. *Cancer Cell*, doi:10.1016/j.ccell.2021.10.009 (2021).
- 26 Zhang, Y. *et al.* Single-cell analyses reveal key immune cell subsets associated with response to PD-L1 blockade in triple-negative breast cancer. *Cancer Cell*, doi:10.1016/j.ccell.2021.09.010 (2021).
- 27 Ayers, M. *et al.* IFN- γ -related mRNA profile predicts clinical response to PD-1 blockade. *J Clin Invest* **127**, 2930-2940, doi:10.1172/jci91190 (2017).
- 28 Schulte-Schrepping, J. *et al.* Severe COVID-19 Is Marked by a Dysregulated Myeloid Cell Compartment. *Cell* **182**, 1419-1440.e1423, doi:10.1016/j.cell.2020.08.001 (2020).
- 29 Zhang, Q. *et al.* Landscape and Dynamics of Single Immune Cells in Hepatocellular Carcinoma. *Cell* **179**, 829-845.e820, doi:10.1016/j.cell.2019.10.003 (2019).
- 30 Groom, J. R. & Luster, A. D. CXCR3 ligands: redundant, collaborative and antagonistic functions. *Immunol Cell Biol* **89**, 207-215, doi:10.1038/icb.2010.158 (2011).
- 31 Hiam-Galvez, K. J., Allen, B. M. & Spitzer, M. H. Systemic immunity in cancer. *Nat Rev Cancer* **21**, 345-359, doi:10.1038/s41568-021-00347-z (2021).
- 32 Ramos-Casals, M. *et al.* Immune-related adverse events of checkpoint inhibitors. *Nat Rev Dis Primers* **6**, 38, doi:10.1038/s41572-020-0160-6 (2020).
- 33 Xu, C. *et al.* Comparative safety of immune checkpoint inhibitors in cancer: systematic review and network meta-analysis. *Bmj* **363**, k4226, doi:10.1136/bmj.k4226 (2018).
- 34 Suresh, K. *et al.* The alveolar immune cell landscape is dysregulated in checkpoint inhibitor pneumonitis. *J Clin Invest* **129**, 4305-4315, doi:10.1172/JCI128654 (2019).
- 35 Suresh, K., Naidoo, J., Lin, C. T. & Danoff, S. Immune Checkpoint Immunotherapy for Non-Small Cell Lung Cancer: Benefits and Pulmonary Toxicities. *Chest* **154**, 1416-1423,

doi:10.1016/j.chest.2018.08.1048 (2018).

36 Delaunay, M. *et al.* Immune-checkpoint inhibitors associated with interstitial lung disease in cancer patients. *Eur Respir J* **50**, doi:10.1183/13993003.00050-2017 (2017).

37 Reuss, J. E., Suresh, K. & Naidoo, J. Checkpoint Inhibitor Pneumonitis: Mechanisms, Characteristics, Management Strategies, and Beyond. *Curr Oncol Rep* **22**, 56, doi:10.1007/s11912-020-00920-z (2020).

38 Bradley, B. *et al.* Interstitial lung disease guideline: the British Thoracic Society in collaboration with the Thoracic Society of Australia and New Zealand and the Irish Thoracic Society. *Thorax* **63 Suppl 5**, v1-58, doi:10.1136/thx.2008.101691 (2008).

39 Rouanne, M., Arpaia, N. & Marabelle, A. CXCL13 shapes tertiary lymphoid structures and promotes response to immunotherapy in bladder cancer. *Eur J Cancer* **151**, 245-248, doi:10.1016/j.ejca.2021.03.054 (2021).

40 Zhang, L. *et al.* Lineage tracking reveals dynamic relationships of T cells in colorectal cancer. *Nature* **564**, 268-272, doi:10.1038/s41586-018-0694-x (2018).

41 Cui, P. *et al.* Association of immune-related pneumonitis with the efficacy of PD-1/PD-L1 inhibitors in non-small cell lung cancer. *Ther Adv Med Oncol* **12**, 1758835920922033, doi:10.1177/1758835920922033 (2020).

42 Overacre-Delgoffe, A. E. & Vignali, D. A. A. Treg Fragility: A Prerequisite for Effective Antitumor Immunity? *Cancer Immunol Res* **6**, 882-887, doi:10.1158/2326-6066.Cir-18-0066 (2018).

43 Mathios, D. *et al.* Anti-PD-1 antitumor immunity is enhanced by local and abrogated by systemic chemotherapy in GBM. *Sci Transl Med* **8**, 370ra180, doi:10.1126/scitranslmed.aag2942 (2016).

44 Peng, Q. *et al.* PD-L1 on dendritic cells attenuates T cell activation and regulates response to immune checkpoint blockade. *Nat Commun* **11**, 4835, doi:10.1038/s41467-020-18570-x (2020).

45 Hao, Q., Vadgama, J. V. & Wang, P. CCL2/CCR2 signaling in cancer pathogenesis. *Cell Commun Signal* **18**, 82, doi:10.1186/s12964-020-00589-8 (2020).

46 Cheng, S. *et al.* A pan-cancer single-cell transcriptional atlas of tumor infiltrating myeloid cells. *Cell* **184**, 792-809.e723, doi:10.1016/j.cell.2021.01.010 (2021).

47 Naidoo, J. *et al.* A Multidisciplinary Toxicity Team for Cancer Immunotherapy-Related Adverse Events. *J Natl Compr Canc Netw* **17**, 712-720, doi:10.6004/jnccn.2018.7268 (2019).

48 Stuart, T. *et al.* Comprehensive Integration of Single-Cell Data. *Cell* **177**, 1888-1902.e1821, doi:10.1016/j.cell.2019.05.031 (2019).

- 49 McGinnis, C. S., Murrow, L. M. & Gartner, Z. J. DoubletFinder: Doublet Detection in Single-Cell RNA Sequencing Data Using Artificial Nearest Neighbors. *Cell Systems* **8**, 329-337.e324, doi:10.1016/j.cels.2019.03.003 (2019).
- 50 Trapnell, C. *et al.* The dynamics and regulators of cell fate decisions are revealed by pseudotemporal ordering of single cells. *Nature biotechnology* **32**, 381-386, doi:10.1038/nbt.2859 (2014).
- 51 Street, K. *et al.* Slingshot: cell lineage and pseudotime inference for single-cell transcriptomics. *BMC Genomics* **19**, 477, doi:10.1186/s12864-018-4772-0 (2018).
- 52 Hänzelmann, S., Castelo, R. & Guinney, J. GSVA: gene set variation analysis for microarray and RNA-Seq data. *BMC bioinformatics* **14**, 7, doi:10.1186/1471-2105-14-7 (2013).
- 53 Jin, S. *et al.* Inference and analysis of cell-cell communication using CellChat. *Nature communications* **12**, 1088, doi:10.1038/s41467-021-21246-9 (2021).

Figures

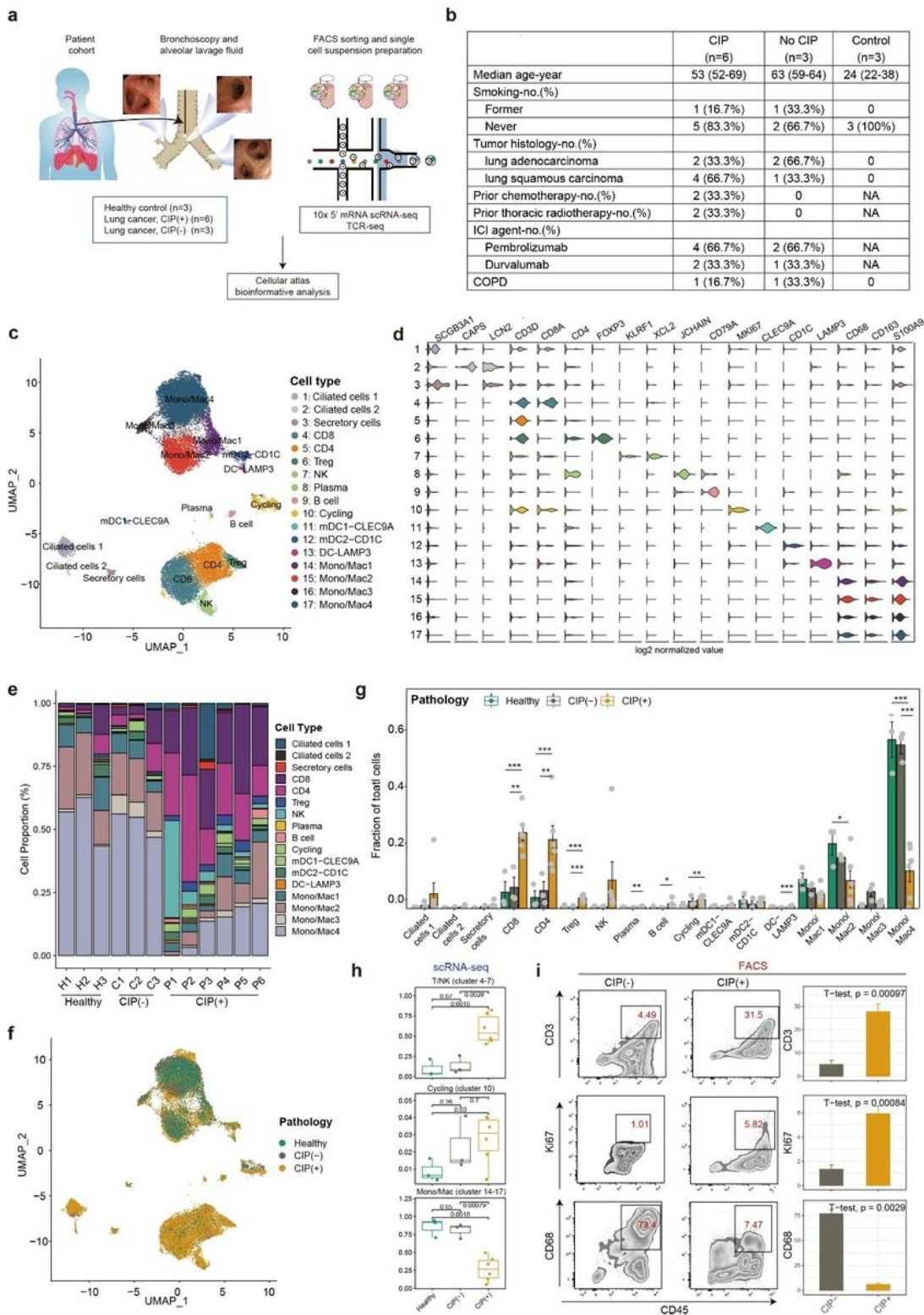


Figure 1

Global analysis of immune cell populations in CIP. a A general workflow of BALF collection and processing of single-cell suspensions for scRNA-seq and flow cytometry. **b** Summary of patient cohorts for scRNA-seq analysis. **c, d** Unbiased clustering (**c**) and cell type annotation **d** of 78,027 high-quality BALF cells. **e** The proportion of cell types in each sample. **f** The distribution of 78,027 high-quality BALF cells in distinct pathology samples. **g** Relative contribution of each cell type in distinct pathology

CIP associated CD8⁺ T Cell with cytotoxicity programs. **a** Sub-clustering of CD8⁺ T cells revealed eight cell-subclusters. **b** The top 10 differentially expressed genes among eight CD8⁺ cell-subclusters. **c** The proportion of eight CD8⁺ cell-subclusters in each sample. **d** Relative contribution of eight CD8⁺ cell-subclusters in distinct sample pathology. *P* values were assessed by Wilcoxon test. **P* < 0.05, ***P* < 0.01, ****P* < 0.001. **e** CIP associated CD8⁺ T frequencies as determined by flow cytometry (percentage of live CD8⁺ cells). *P* values were assessed by Student t test. **f** Violin plots showing the expression of immune checkpoint molecules, split by sample pathology. **g** Box plots showing the expression of T cell cytotoxic and effector genes in CIP associated cells compared than others. *P* values were assessed by Wilcoxon test. **h** DEGs of CD8⁺ T cell cluster in CIP(+) compared than healthy (left panel) and CIP(-) (right panel). **i** The pseudotime analysis for CD8 subtypes determined by Slingshot. **j** Visualization of TCR clonotypes identified in CD8-ZNF683 (CD8-Trm) and CIP-associated CD8⁺ T clusters.

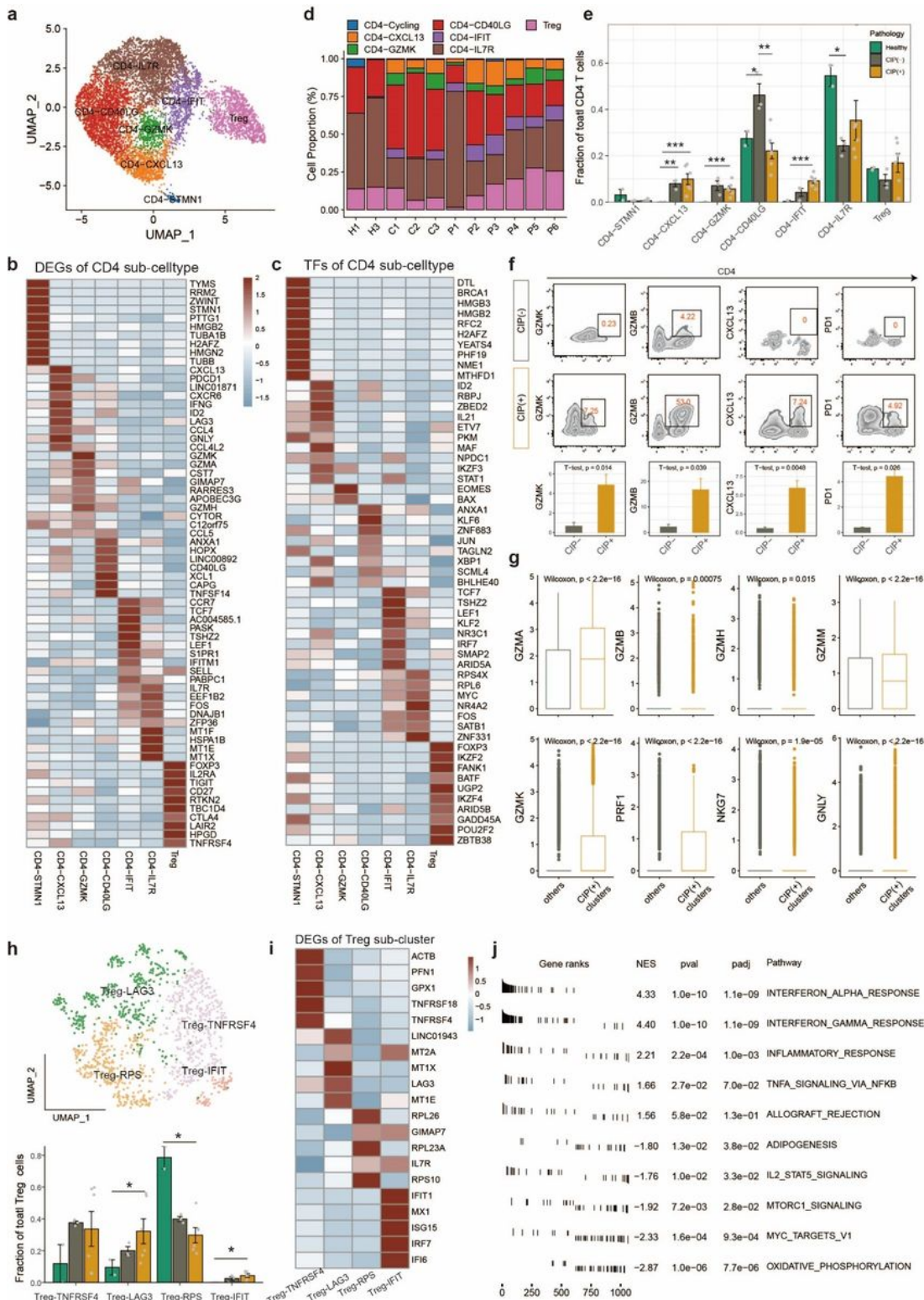


Figure 3

CIP associated CD4⁺ T Cell with cytotoxicity programs. **a** Sub-clustering of CD4⁺ T cells revealed seven cell-subclusters. **b** The top 10 differentially expressed genes among seven CD4⁺ cell-subclusters. **c** The top 10 differentially transcriptomic factors (TFs) among seven CD4⁺ cell-subclusters. **d** The proportion of seven CD4⁺ cell-subclusters in each sample. **e** Relative contribution of seven CD4⁺ cell-subclusters in

distinct sample pathology. *P* values were assessed by Wilcoxon test. **P* < 0.05, ***P* < 0.01, ****P* < 0.001. **f** CIP associated CD4⁺ T frequencies as determined by flow cytometry (percentage of live CD4⁺ cells). *P* values were assessed by Student t test. **g** Box plots showing the expression of T cell cytotoxic and effector genes in CIP associated CD4⁺ T cells compared than others. *P* values were assessed by Wilcoxon test. **h** Sub-clustering of Treg cells revealed four cell-subclusters and relative contribution of four Treg cell-subclusters in distinct sample pathology. *P* values were assessed by Wilcoxon test. **P* < 0.05, ***P* < 0.01, ****P* < 0.001. **i** The top 5 DEGs among four Treg cell-subclusters. **j** Enriched signaling pathways in CIP(+) associated Treg cells with that of CIP(-). NES, normalized enrichment score.

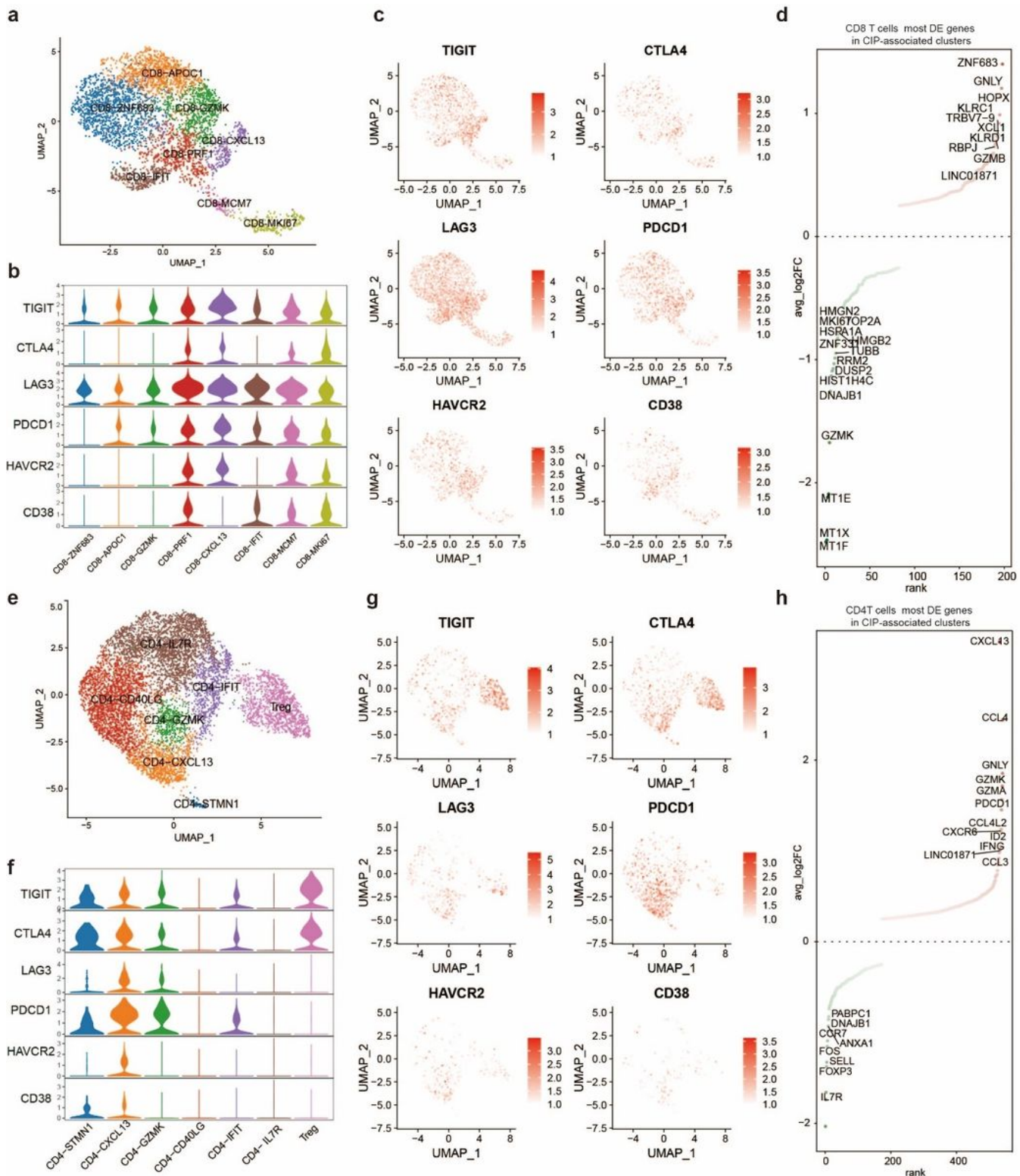


Figure 4

Analysis of T cell checkpoints and colitis-associated genes. **a-c** The expression of immune checkpoint molecules TIGIT, CTLA4, PDCD1, HAVCR1, and CD38 in CD8⁺ T subclusters. **d** The differentially expressed genes between CIP(+) CD8⁺ cell-subclusters compared with CIP(-) CD8⁺ cell-subclusters. **e-g** The expression of immune checkpoint molecules TIGIT, CTLA4, PDCD1, HAVCR1, and CD38 in CD4⁺ T

subclusters. **h** The differentially expressed genes between CIP(+) CD4⁺ cell-subclusters compared with CIP(-) CD4⁺ cell-subclusters.

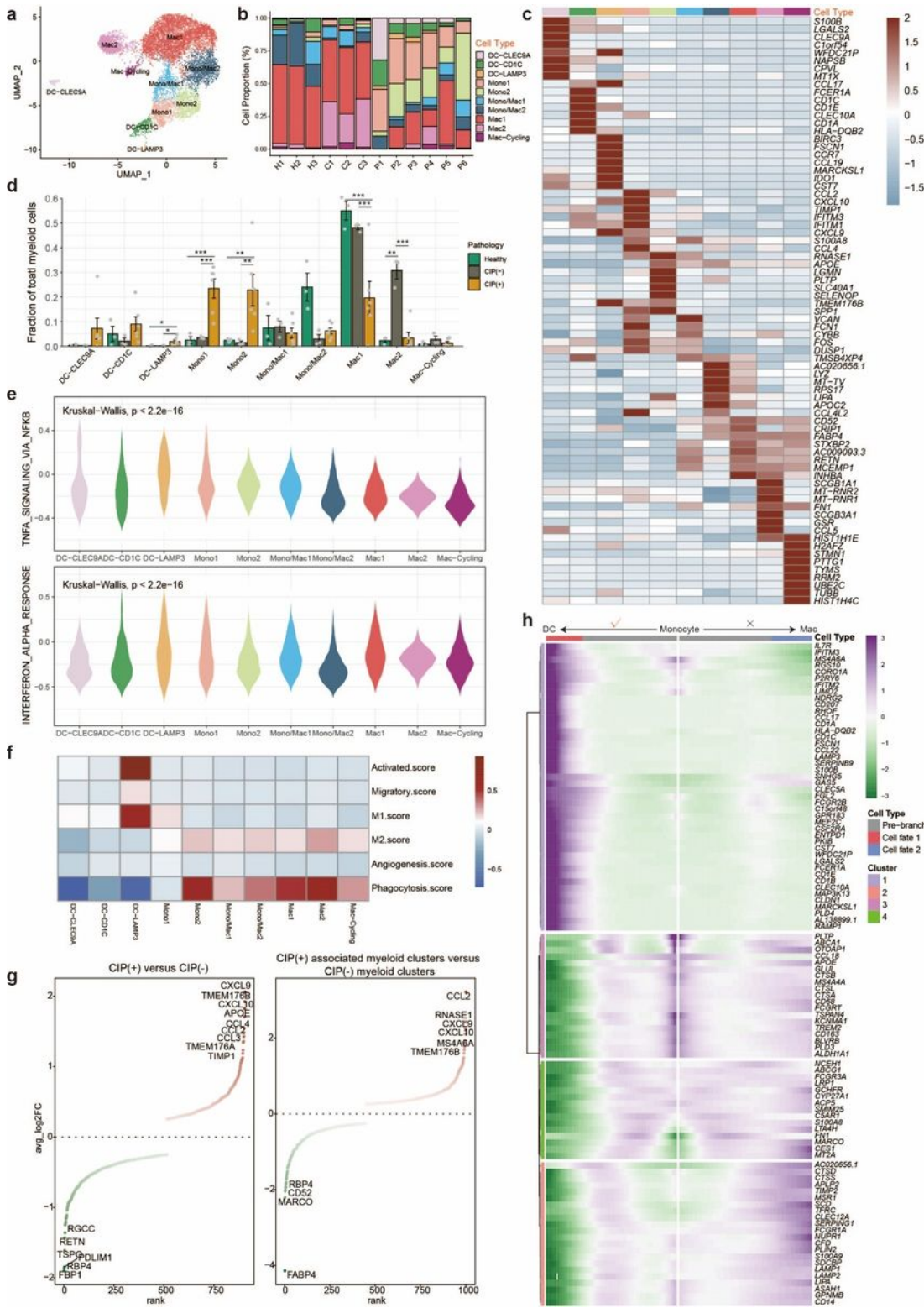


Figure 5

Hyperinflammatory myeloid cells expanded in CIP. a Sub-clustering of myeloid cells revealed ten cell-subclusters. **b** The proportion of ten myeloid cell-subclusters in each sample. **c** The top 10 differentially

expressed genes among ten myeloid cell-subclusters. **d** Relative contribution of ten myeloid cell cell-subclusters in distinct sample pathology. *P* values were assessed by Wilcoxon test. **P* < 0.05, ***P* < 0.01, ****P* < 0.001. **e** Expression of inflammatory hallmark genesets in ten myeloid cell cell-subclusters. **f** The expression of M1 (pro-inflammatory), M2 (anti-inflammatory), migratory, angiogenesis, phagocytosis, and activation score in ten myeloid cell cell-subclusters. **g** The differentially expressed genes of CIP(+) myeloid cells (left) and subclusters (right). **h** Heatmap showing the scaled expression of dynamic genes along the monocyte differentiation pseudotime axis.

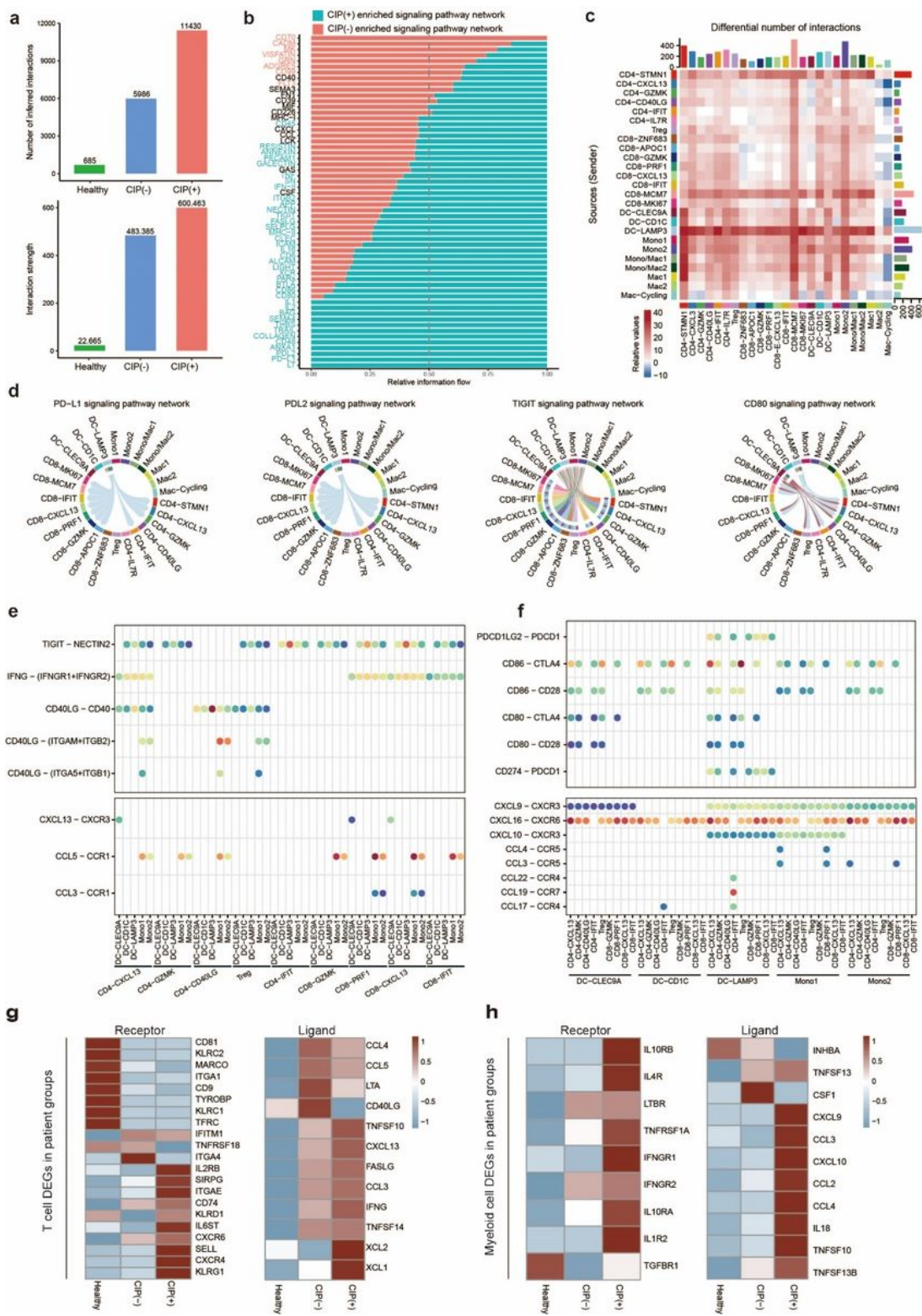


Figure 6

Multi-lineage intercellular crosstalk and potential therapeutic targets for CIP. **a** Number of inferred interactions and scores in distinct BALF sample pathology. **b** Enriched signaling pathway networks between CIP(+) and CIP(-) group. **c** Differential number of interactions in different BALF immune cell subtypes. **d** Enriched immune checkpoint signaling pathway networks in different BALF immune cell subtypes. **e, f** Dot plot showing the communication probability of the indicated ligand-receptor pairs

between CXCL13⁺ T cells and LAMP3-DC. **g, h** Heatmap showing averaged expression of the indicated cytokine and cytokine receptor genes compared among patient groups.

Supplementary Files

This is a list of supplementary files associated with this preprint. Click to download.

- [supplementarytable.docx](#)